J. Fluid Mech. (2012), *vol.* 712, *pp.* 354–383.
doi:10.1017/jfm.2012.426

On the late-time growth of the two-dimensional Richtmyer–Meshkov instability in shock tube experiments

Robert V. Morgan[1]†, R. Aure[1]‡, J. D. Stockero[1]§, J. A. Greenough[2], W. Cabot[2], O. A. Likhachev[1] and J. W. Jacobs[1]

[1] Department of Aerospace and Mechanical Engineering, The University of Arizona, Tucson, AZ 85721, USA

[2] Lawrence Livermore National Laboratory, Livermore, CA 94550, USA

(Received 9 January 2012; revised 29 June 2012; accepted 27 August 2012; first published online 1 October 2012)

In the present study, shock tube experiments are used to study the very late-time development of the Richtmyer–Meshkov instability from a diffuse, nearly sinusoidal, initial perturbation into a fully turbulent flow. The interface is generated by two opposing gas flows and a perturbation is formed on the interface by transversely oscillating the shock tube to create a standing wave. The puncturing of a diaphragm generates a Mach 1.2 shock wave that then impacts a density gradient composed of air and SF_6, causing the Richtmyer–Meshkov instability to develop in the 2.0 m long test section. The instability is visualized with planar Mie scattering in which smoke particles in the air are illuminated by a Nd:YLF laser sheet, and images are recorded using four high-speed video cameras operating at 6 kHz that allow the recording of the time history of the instability. In addition, particle image velocimetry (PIV) is implemented using a double-pulsed Nd:YAG laser with images recorded using a single CCD camera. Initial modal content, amplitude, and growth rates are reported from the Mie scattering experiments while vorticity and circulation measurements are made using PIV. Amplitude measurements show good early-time agreement but relatively poor late-time agreement with existing nonlinear models. The model of Goncharov (*Phys. Rev. Lett.*, vol. 88, 2002, 134502) agrees with growth rate measurements at intermediate times but fails at late experimental times. Measured background acceleration present in the experiment suggests that the late-time growth rate may be influenced by Rayleigh–Taylor instability induced by the interfacial acceleration. Numerical simulations conducted using the LLNL codes Ares and Miranda show that this acceleration may be caused by the growth of boundary layers, and must be accounted for to produce good agreement with models and simulations. Adding acceleration to the Richtmyer–Meshkov buoyancy–drag model produces improved agreement. It is found that the growth rate and amplitude trends are also modelled well by the Likhachev–Jacobs vortex model (Likhachev & Jacobs, *Phys. Fluids*, vol. 17, 2005, 031704). Circulation measurements also show good agreement with

† Email address for correspondence: rvm@email.arizona.edu

‡ Present address: Roxar Flow Measurement, Gamle Forusvei 17, 4065 Stavanger, Norway.

§ Present address: Lockheed Martin Aeronautics, 1011 Lockheed Way, Palmdale, CA 93599.

the circulation value extracted by fitting the vortex model to the experimental data.

Key words: compressible flows, instability, nonlinear instability

1. Introduction

The Richtmyer–Meshkov instability (Richtmyer 1960; Meshkov 1969) is a member of a class of fluid instabilities that occur across density interfaces in fluid media. This instability is very similar to the better-known Rayleigh–Taylor instability (Rayleigh 1900; Taylor 1950) that occurs when an interface is subjected to a constant acceleration such as produced by gravity. The Richtmyer–Meshkov instability, however, occurs when the interface is impulsively accelerated. This instability is a major component of supersonic mixing, and enhances mixing during fuel injection in scramjet propulsion systems (Yang, Kubota & Zukoski 1993). The instability occurs in nature when the helium–hydrogen interface in core-collapse supernovae is subjected to the shock wave generated by the bouncing stellar core (Kifonidis *et al.* 2006). In engineering applications, the Richtmyer–Meshkov instability occurs in inertial confinement fusion when a capsule containing deuterium and tritium is ablated and the heavy and light fuel layers begin to mix. Minimization of mixing of the deuterium–tritium fuel by instabilities is crucial to the successful formation of the fusion reaction's central hot spot (Edwards *et al.* 2011).

In the generation of Richtmyer–Meshkov instability, a perturbed interface is subjected to an impulsive acceleration (often produced by a shock wave), which deposits kinetic energy on the fluid interface and causes perturbations to grow with time. This growth eventually causes the fluids separated by the interface to mix together and become turbulent. This instability is initiated by baroclinic vorticity deposition (as shown in figure 1) when the shock wave, a pressure gradient (∇p), interacts with a density gradient ($\nabla \rho$). The two-dimensional, inviscid vorticity transport equation can be written as

$$\rho \frac{\mathrm{D}}{\mathrm{D}t}\left(\frac{\omega}{\rho}\right) = \frac{1}{\rho^2}\nabla\rho \times \nabla p. \tag{1.1}$$

Thus, the initial vorticity (ω) distribution is generated by the shock wave when there is a misalignment of pressure and density gradients. Additional weak vorticity will also be generated by the transmitted and reflected shock waves, which will be curved due to interaction with the perturbed interface (Huerte Ruiz de Lira, Velikovich & Wouchuk 2011). The deposited vorticity causes the interface to roll up into mushroom-like spikes of heavy fluid penetrating into the light fluid, separated by bubbles of light fluid moving into the heavy fluid (as shown in figure 1). The total amount of vorticity deposited by the shock wave determines the growth rate of the instability. The spikes and bubbles continue to grow and the vorticity rolls up into regions of concentrated vorticity of alternating sign. Later in the development of the instability, the misalignment of the centripetal acceleration of the vortex cores and the interfacial density gradient causes the generation of additional vorticity (Peng, Zabusky & Zhang 2003). The rolling up of the vorticity will also generate shear on the thin arms of the mushroom structure, leading to the growth of a secondary instability. Over time, this

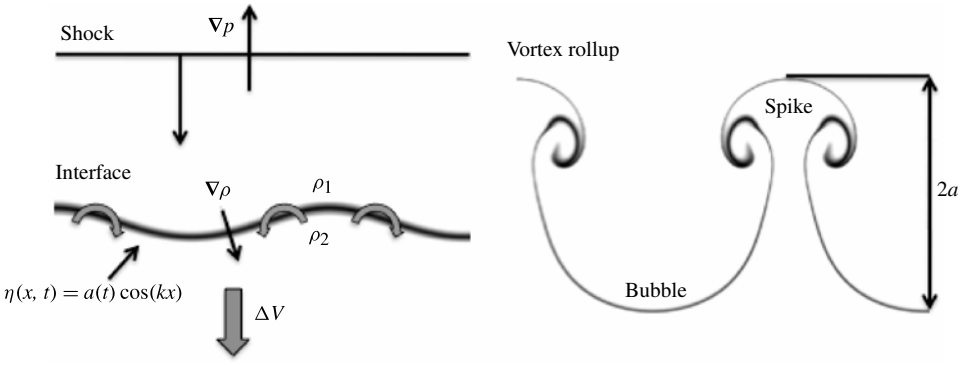

FIGURE 1. Explanation of the deposition of baroclinic vorticity on the interface. (*a*) The shock wave travels downward toward the interface and applies a pressure gradient across the density gradient which generates baroclinic vorticity on the interface. (*b*) This baroclinic vorticity rolls up into spikes of heavy fluid separating bubbles of light fluid as the interface travels down the shock tube with the mean post-shock flow.

secondary instability eventually becomes turbulent, and the mushroom structures begin to disintegrate as the stems thin and the arms mix due to turbulent diffusion.

The Richtmyer–Meshkov instability was initially modelled by Richtmyer (1960), by replacing gravity in the linear stability theory of Taylor (1950) with an impulsive acceleration in the form of a Dirac delta function, resulting in

$$a(t) = a_0[1 + kA\Delta Vt], \tag{1.2}$$

which describes the growth of the perturbation amplitude a, where k is the wavenumber of the initial disturbance, ΔV is the velocity change of the interface due to impulsive acceleration, and A is the Atwood number defined by

$$A = \frac{\rho_2 - \rho_1}{\rho_2 + \rho_1}, \tag{1.3}$$

where ρ_2 is the density of the lower fluid and ρ_1 is the density of the upper fluid. Richtmyer further observed that for the light-to-heavy configuration post-shock values of a_0 and A produced the best agreement with numerical simulations, while for the heavy-to-light configuration Meyer & Blewett (1972) observed that the average of pre-shock and post-shock values of a_0 worked best. While there have been a number of more recent studies aimed at incorporating more realistic physics into this simple linear stability analysis (Wouchuk & Nishihara 1997; Krechetnikov 2009), linear stability theory is, nevertheless, accurate for only a very brief time following shock interaction. As a result there have been a number of attempts to extend Richtmyer's linear solution into the nonlinear regime (Nishihara *et al.* 2010). For example Zhang & Sohn (1997*a*), and others (Vandenboomgaerde, Gauthier & Mügler 2002; Matsuoka, Nishihara & Fukuda 2003), have focused on weakly nonlinear analyses. These types of analysis extend the linear solution a bit farther in time. However, they still fail to effectively model the instability at moderate to late times. Other types of analysis use potential flow to model the late-time motion of the bubble and spike tips (Goncharov 2002; Mikaelian 2003; Herrmann, Moin & Abarzhi 2008). However, the most successful models are those that are semi-empirical in nature: for example, see the models of Sadot *et al.* (1998), Likhachev & Jacobs (2005), and Dimonte &

Ramaprabhu (2010). In addition to theoretical analyses, there have been a number of studies using numerical simulations to model the late-time instability (Holmes *et al.* 1999; Schilling, Latini & Don 2007). Note that the term 'late-time' is used here to refer to the single-mode instability, which is distinguished from recent work focused on simulating the multimode, fully turbulent instability (Grinstein, Gowhardhan & Wachtor 2011; Hahn *et al.* 2011; Lombardini *et al.* 2011; Thornber *et al.* 2011).

The Richtmyer–Meshkov instability was first observed experimentally by Meshkov (1969). These early experiments used a thin membrane (Vetter & Sturtevant 1995; Prasad *et al.* 2000) to separate the two test gases prior to the impact of the shock wave. This method is still in use today despite the fact that pieces of the membrane become entrained in the fluid impeding flow visualization. In addition, it has been found that in the light-to-heavy configuration, particles from the membrane will remain on the interface and reduce the linear growth rate of the instability (Mariani *et al.* 2008). Other studies have used explosive drivers to ablate easily liquefiable metal with machined initial perturbations (Benjamin, Trease & Shaner 1984). Another experimental technique involves extracting a plate that initially separates the interfacial fluids, using the wake it creates as the initial perturbation (Bonazza & Sturtevant 1996). A membraneless approach was developed, using gas cylinders deposited by a laminar jet, to develop well-characterized diffuse initial conditions (Jacobs 1993). This technique was then extended by using a varicose gas curtain to develop a thin layer initial perturbation (Jacobs *et al.* 1993, 1995). This technique is still in use at the Los Alamos National Laboratory (Balakumar *et al.* 2008; Tomkins *et al.* 2008).

Jones & Jacobs (1997) first used the novel technique of using a stagnating flow of gases exiting from slots in the sidewall of the shock tube to create a well-defined initial interface. This technique was further employed by Collins & Jacobs (2002) and Jacobs & Krivets (2005). In these experiments the initial perturbation was created by gently oscillating the shock tube back and forth, creating a standing sinusoidal wave on the interface. The time scale associated with the standing wave is orders of magnitude longer than the time scale associated with the propagation of the shock wave. Therefore, during the experiment, the initial perturbation can be considered static. This technique is currently in use at The University of Arizona, and has most recently been implemented by the Wisconsin Shock Tube Laboratory via moving plates that push and pull the fluid at the interface in a rigid shock tube (Motl *et al.* 2007).

Since the first work on this subject, the experiments at the University of Arizona have evolved by making improvements in visualization capability, such as by implementing planar-laser-induced fluorescence (PLIF) (Collins & Jacobs 2002) and most recently particle image velocimetry (PIV) (Aure & Jacobs 2008). In addition, attempts have been made to extend the observation time farther into the nonlinear regime (Jacobs & Krivets 2005).

One major shortcoming encountered in these previous shock tube experiments was the inability to acquire multiple images from a single experiment. Due to the variation in initial conditions from experiment to experiment, the scatter in the data was significant. The current study employs high-speed video imaging to capture a sequence of images from a single experiment. Hence, the initial perturbation is well characterized and the time history of the instability is observed. This time history causes relatively little scatter in the data and time derivatives can be extracted. In addition to the improved data acquisition capability, the experiments reported here use a much longer shock tube, thus allowing the observation of the instability at much later times prior to re-shock. Thus, the current study represents our best effort to date,

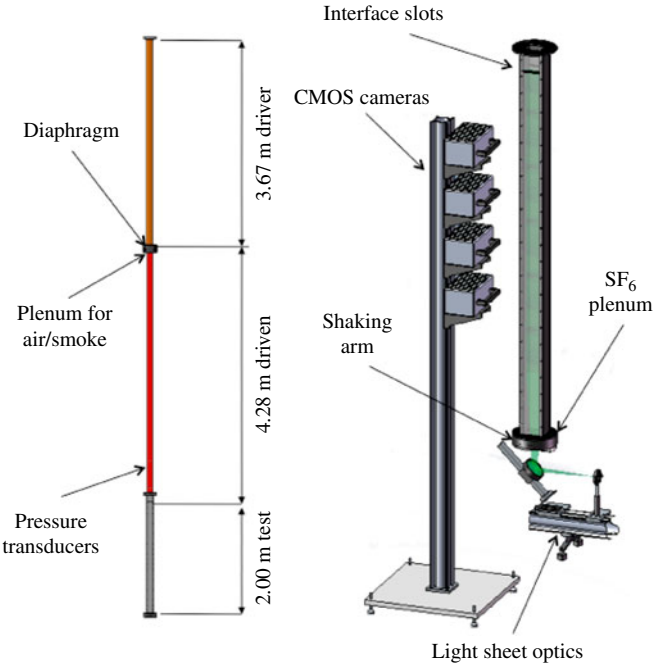

FIGURE 2. (Colour online) The University of Arizona 10 m vertical shock tube used for the present study: (*a*) scale diagram demonstrating the overall length of the shock tube, (*b*) the test section and visualization optics. The length of the test section maximizes the amount of time before re-shock occurs, while the large driver section delays the onset of the reflected expansion wave. The major difference between this setup and the particle imaging velocimetry setup is that one CCD camera on a rail system is utilized for PIV instead of the four CMOS cameras depicted in (*b*).

in that it employs our new capability to measure the growth of the instability. In addition, it extends our experimental durations by a factor of three over our previous studies.

2. Experimental setup

2.1. *Shock tube*

Experiments were performed using the 10 m shock tube at the University of Arizona. Details of previous research using this shock tube can be found in Aure & Jacobs (2008). Figure 2 shows two diagrams of the shock tube: the complete shock tube to scale (figure 2*a*) and the test section and visualization optics (figure 2*b*). The shock tube has a 3.7 m driver section, a 6.3 m driven section, and a 2.0 m test section with a 88.9 mm square cross-section. The driven section is separated by two to three polypropylene diaphragms and is pressurized using nitrogen gas. When the pressure in the driver section reaches the desired value a solenoid is activated which plunges an arrowhead made from four X-acto knife blades into the diaphragm. The blades puncture the diaphragm, sending a shock wave travelling down the shock tube. The shock wave impacts the air–SF_6 interface, and the Richtmyer–Meshkov instability develops in the test section. Figure 3 shows the interaction of the waves generated by the rupturing of the diaphragm in the shock tube.

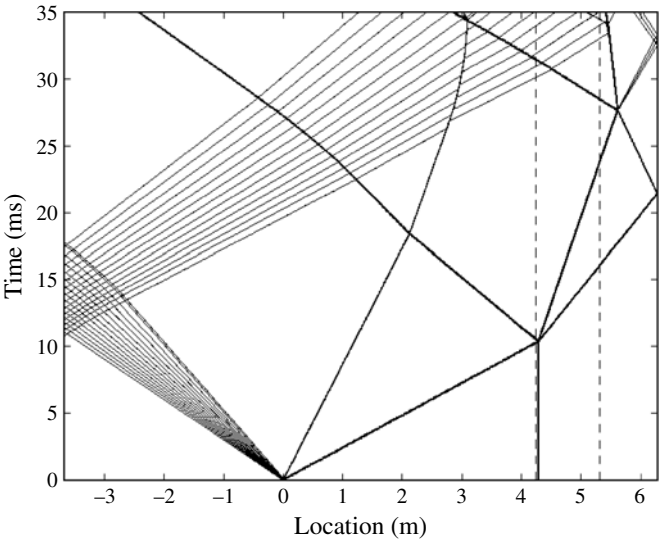

FIGURE 3. An x versus t diagram for the shock tube used in the present study. The dashed lines indicate the test area actually imaged by the cameras. This diagram shows the long test time available before reflected waves reach the interface.

The interface is created between air entering through a plenum at the top of the driven section and SF_6 entering through a similar plenum at the bottom of the test section at matched flow rates of $6\ \mathrm{l\ min^{-1}}$. The opposing flows of gas are allowed to exit through two 6.4 by 88.9 mm slots at the front and back of the top of the test section creating a flat interfacial stagnation flow. After this flat interface is established, a stepper motor gently oscillates the flexible shock tube at a prescribed frequency to create a standing wave. Due to the perturbation formation method, only $n + 1/2$ wavelengths, where $n = 1, 2, 3,$ can be generated across the shock tube width. When the shock wave impacts the interface, the interface is in the shape of a two-dimensional sinusoidal wave, which becomes the initial perturbation for the experiment.

The experiment is initialized by synchronizing a signal from an optical switch attached to the stepper motor to a handset switch controlled by the operator. When both switches are simultaneously closed, the solenoid plunger is activated. As the shock wave travels down the shock tube, it passes two PCB Piezotronics 112A22 high-resolution, dynamic, ICP pressure transducers located 273 and 732 mm above the interface. Both pressure transducers are connected to an Agilent 225 MHz Universal Counter while the second is also used to trigger a Stanford Research Systems DG535 digital delay generator. The delay generator employs a prescribed delay before triggering the start of an image acquisition sequence. Experiments are illuminated by laser-light entering the test section through a fused silica window in the bottom of the shock tube.

2.2. *Particle image velocimetry*

In the PIV experiments, the light and heavy gases are seeded using custom-built atomizers that atomize a suspension of 0.30 μm polystyrene latex spheres suspended in distilled water (Liu & Lee 1975). The concentration of latex spheres in the solution determines the seeding density in the gas. Water is removed from the seeded gas flow

using desiccant driers located between the atomizers and the shock tube plenums. The seeding densities of the gas flows are matched and optimized visually by adjusting the suspension particle concentrations.

One double-exposed image per experiment is obtained by illuminating the seeded flow using a dual cavity pulsed Nd:YAG laser. The laser beam is focused using 1677.0 and 1118.1 mm spherical lenses and expanded to a 1 mm thick light sheet using −165.6 and −220.7 mm cylindrical lenses. Experimental images are captured using a thermoelectrically cooled CCD camera with 1250 pixel × 1152 pixel resolution and a Nikon 60 mm f/2.8D macro lens. To enhance the signal-to-noise ratio of the data and to minimize noise from reflections and scattering of light from the shock tube walls, the walls are painted with a mixture of clear varnish and Rhodamine 6G. When the green laser light is absorbed by the walls, it is weakly emitted in the yellow-to-red spectrum ($\lambda > 545$ nm). The yellow/red light emitted from the shock tube walls is filtered out by an optical bandpass filter ($\lambda = 532 \pm 5$ nm) attached to the camera lens.

The processing of particle images is implemented using LaVision's DaVis FlowMaster software. Image processing is done using a three-step multipass autocorrelation algorithm with a decreasing window size. The initial pass utilizes a normalized second-order correlation function and 64 pixel × 64 pixel interrogation windows with 50 % overlap. The final two passes utilize a normalized correlation function and 32 pixel × 32 pixel interrogation windows with 50 % overlap (Keane & Adrian 1990, 1991). A liberal restriction was put on the allowable vector range and a median filter was applied after the final pass. Empty cells were filled with interpolated vectors. Optimal Δt_{PIV} and processing parameters were determined based on known theory and optimized experimentally (Westerweel 1993; Raffel, Kompenhans & Willert 1998). The raw data were analysed using MATLAB to extract vorticity, circulation, and growth rates.

2.3. *Planar Mie scattering*

Planar Mie scattering experiments are visualized by seeding the light gas with incense smoke. Incense smoke and air are added at the top of the driven section and are allowed to displace the air in the driven section. The smoke is visualized by a light sheet created by a 50 mm focal length collimating lens, a 600 mm focal length focusing lens, and a 2000 mm focal length cylindrical lens. A high flashing frequency Photonics Industries model DM50-527 diode pumped Nd:YLF laser operating at a wavelength of 527 nm is used for illumination. Scattered light from smoke particles is recorded by four Photron Fastcam-APX RS cameras with Nikon 50 mm f/1.2 lenses operating at a resolution of 512 pixels × 1024 pixels at 6 kHz.

Acquisition timing is controlled by a LaVision HSC external timing board. Data are acquired using the DaVis software by LaVision GmbH. The delay generator waits 0.3 ms before triggering the HSC to start recording images. Upon receiving the trigger signal, the HSC sends synchronized signals to the laser control unit and high-speed cameras. Image data were calibrated in DaVis using an image of a linear scale located at the centre of the laser plane for all of the cameras.

Each camera's field of view overlaps with its neighbour's by ≈1 cm. In order to maximize the number of data points measured and ultimately create videos of the instability the images are spliced together. The splicing was accomplished using a number of MATLAB routines using tools found in the image processing toolbox and DaVis macros. The MATLAB routines straighten the images, splice them across cameras, and scale their intensities to match across cameras. Measurements are made visually and have an error of $\leqslant \pm 0.54$ mm.

3. Numerical simulation methods

3.1. *Miranda*

The Miranda code is a research hydrodynamics code developed at Lawrence Livermore National Laboratory (LLNL). The compressible version of the Miranda code (Cook & Cabot 2005; Cook 2007) used solves the Navier–Stokes equations for compressible ideal gases. In order to capture the effects of small scales on the problem, grid-dependent artificial viscosities and diffusivity are used. The governing equations are solved using a fourth-order Runge–Kutta scheme in time, and a tenth-order compact scheme for spatial derivatives (Cook & Cabot 2005). More details on the accuracy of the scheme used for solving the differential equations are given in Cook & Cabot (2004) and Cook (2007).

The setup for the problem in Miranda simulates the instability starting from a pure cosine wave initial perturbation. In the x direction, periodic boundary conditions are used to mimic an endless row of developing mushrooms. In the z direction an outflow boundary condition is used which allows most waves to exit the domain. The simulation uses a frame of reference travelling downward at the post-shock unperturbed interface velocity. Thus, when the problem is initiated, the interface appears to travel upward at the velocity induced by the shock wave (as found in a one-dimensional simulation). The shock wave is initiated 2 wavelengths above the interface and travels downward.

Once the shock wave and interface interact, the unperturbed interface location is frozen in the moving frame of reference. The perturbed simulations have bubbles and spikes that grow from the fixed unperturbed interface position. The shock waves that reflect and refract from the interface are removed from the computational domain to avoid any spurious reflections that they may cause at the boundaries. This is done by removing the small pieces of computational domain near the boundaries in which they reside and enforcing outflow boundary conditions at the post-shock states. The final computational domain is 6 wavelengths long by 1 wavelength across with the unperturbed interface location residing 2 wavelengths from the bottom of the domain (allowing sufficient numerical domain for the spike to grow into). The resolution of the simulation is 256 grid points per wavelength on a square mesh. Convergence was checked by performing simulations at 256 and 512 grid points per wavelength where it was found that the higher-resolution simulation produced only a 0.04 % change in the instability amplitude.

The initial perturbation is a pure cosine wave

$$z_{int} = z_0 - a_0 \cos(kx) \tag{3.1}$$

with a wavenumber

$$k = \frac{2\pi\left(n + \frac{1}{2}\right)}{88.9 \text{ mm}} \tag{3.2}$$

estimated based on the width of the physical shock tube, where z_0 is the mean location of the interface and z_{int} is the location of the interface. The diffusion profile used is an error function such that

$$Y_1 = \frac{1}{2} + \frac{1}{2}\text{erf}\left(\frac{\sqrt{\pi}(z - z_{int})}{\delta}\right), \tag{3.3}$$

where Y_1 is the species mass fraction of fluid 1, the error function is approximated as found by Abramowitz & Stegun (1964), and δ is the maximum slope thickness.

The values used for maximum slope thicknesses were measured in PLIF experiments. Shock wave strengths were estimated based on the mean interface velocity that the shock wave induced in the experiments. This step is necessary as the interface generation slots reduce the effective Mach number of the incident shock wave. All of the computational parameters were taken as the mean of the experimental parameters of four experiments.

Amplitude data are extracted using the LLNL VisIt visualization software. Since the transverse location of the bubbles and spikes do not move in these simulations, line-outs are used to determine the 50 % mass fraction points. The amplitude is calculated as half of the distance along the shock tube between the 50 % mass fraction points that make up the bubble and spike. Circulation is extracted by area, integrating the two-dimensional vorticity over a box that includes one half-wavelength of the instability and extends to the edges of the simulation.

3.2. *Ares*

Ares is an arbitrary Lagrangian–Eulerian (ALE) hydrodynamics code developed at LLNL (see McFarland, Greenough & Ranjan 2011). The Lagrange time advancement is second-order predictor–corrector and uses the Gauss divergence theorem to give the discrete finite difference equations (Wilkins 1963). The Lagrange scheme operates on a staggered mesh where velocities are defined at nodes and the density and energy are defined at zone centres. All numerical differences are fully second-order in space. Artificial viscosity is used to suppress spurious oscillations following the method of Kolev & Rieben (2009). The remap phase of the calculation, where the Lagrangian solution is remapped back to a non-Lagrangian mesh, is fully second-order. The original method is given by Sharp & Barton (1981).

The setup for the Ares problems starts with a pure cosine wave initial perturbation, and unlike in the Miranda simulations, the full width of the shock tube is simulated. The diffuseness of the initial interface is modelled with the same error function profile as in Miranda. The full 2.0 m length of the test section is used with the shock wave starting 10.0 cm above the interface. A reflection region 410.0 cm long is set up above the interface to prevent spurious waves from interacting with the developing interface. The bottom, left, and right walls of the shock tube are set as zero normal velocity enforcing the no-penetration condition. Since the full shock tube width is simulated, boundary layers that approximately simulate those seen in experiments can be developed. The boundary layer simulations use a simple constant viscosity model for constructing the viscous stress, and the boundary conditions in these simulations are imposed as solid, no-slip, insulated walls. The top boundary condition is input as a set of sources at the post-shock conditions. Adaptive mesh refinement with four levels of refinement by factors of 3 is used to resolve the interface, the boundary layer entrainment, and the incident shock wave. This results in a resolution of $\sim$218 points per wavelength. Convergence was checked by performing simulations at up to four levels of refinement, where it was found that the highest-resolution simulation produced only a 2.4 % variation in the post-shock interface velocity.

Amplitude data extraction becomes more complicated when boundary layers are present, as the location of the point of maximum spike amplitude begins to move in the transverse direction. Amplitudes were extracted by finding the maximum and minimum points of the 50 % contour (within a window that excludes the boundary layer entrainment region). Circulation is extracted by area, integrating the two-dimensional vorticity over a box containing one half-wavelength of the instability

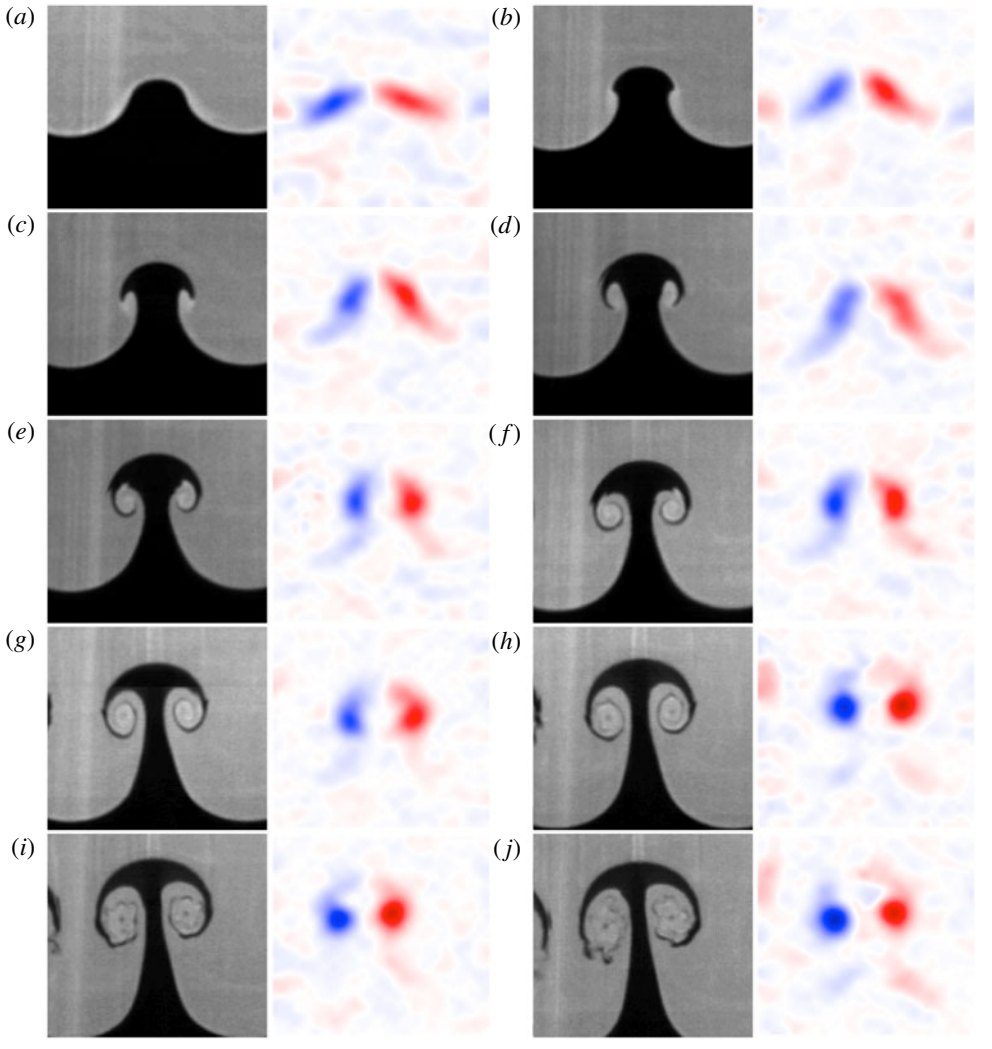

FIGURE 4. (Colour online) A montage of images comparing planar Mie scattering images to PIV vorticity images at (*a*) $t = 0.5$ ms, (*b*) $t = 1.0$ ms, (*c*) $t = 1.5$ ms, (*d*) $t = 2.0$ ms, (*e*) $t = 2.5$ ms, (*f*) $t = 3.0$ ms, (*g*) $t = 3.5$ ms, (*h*) $t = 4.0$ ms, (*i*) $t = 4.5$ ms, and (*j*) $t = 5.0$ ms. The vorticity can be seen to roll up into concentrated centres of vorticity as the instability develops.

and excluding the boundary layer. The box is centred at the average interface location and extends far beyond the interface (80 cm in each direction).

4. Results

4.1. *Experimental results*

The sequence of images displayed in figures 4 and 5 shows a planar Mie scattering experiment compared to vorticity maps obtained from separate PIV experiments chosen to have matching conditions. In these images only one wavelength of a 2.5-wavelength experiment is shown. The first frame shows the instability during the linear

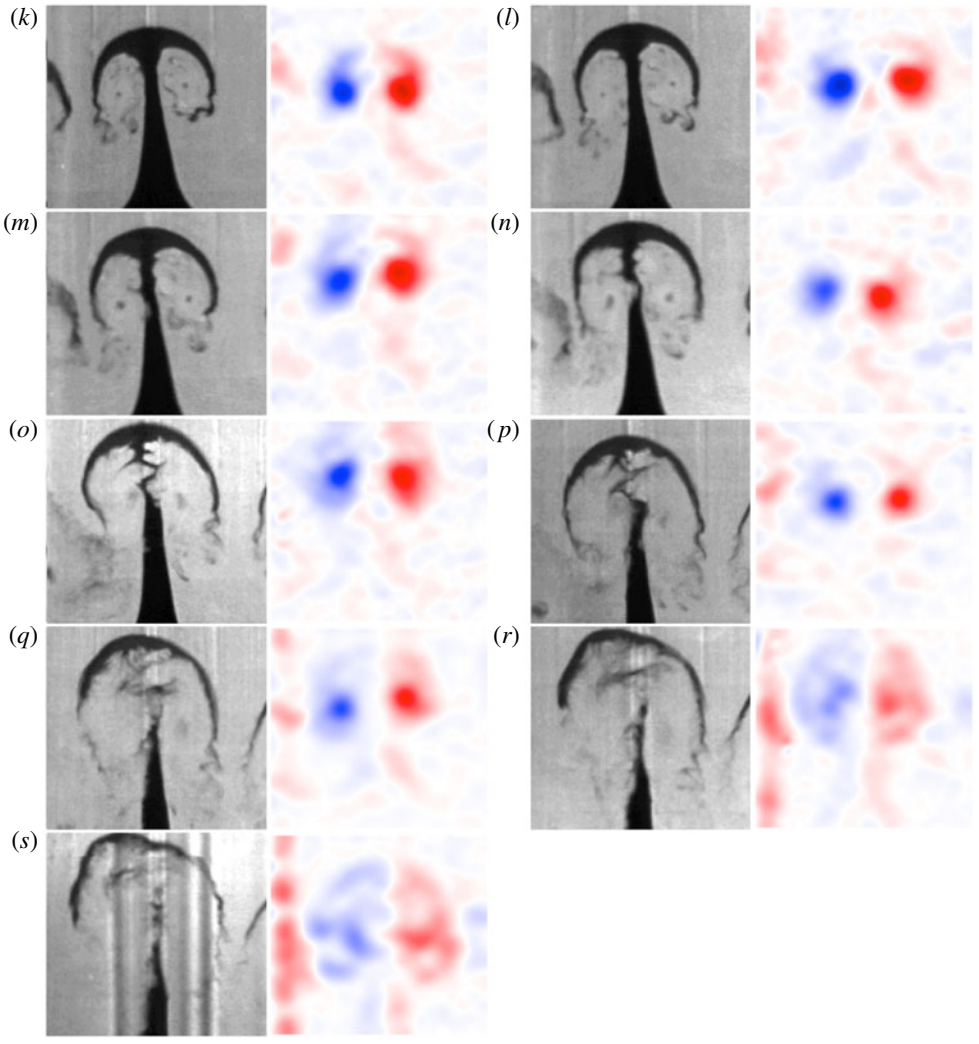

FIGURE 5. (Colour online) Continued montage of images comparing planar Mie scattering images to PIV vorticity images at (*k*) $t = 5.5$ ms, (*l*) $t = 6.0$ ms, (*m*) $t = 6.5$ ms, (*n*) $t = 7.0$ ms, (*o*) $t = 8.0$ ms, (*p*) $t = 9.0$ ms, (*q*) $t = 10.0$ ms, (*r*) $t = 11.0$ ms, and (*s*) $t = 12.0$ ms. The vorticity is seen to disperse as the secondary instability breaks up the mushroom structures.

growth phase, with the initial vorticity distribution created from the passage of the shock wave through the diffuse interface. From 1.0 to around 2.0 ms, the interface becomes multivalued and enters the nonlinear phase. In these images, vorticity is advected into areas of concentrated vorticity. From 2.5 to 3.5 ms the concentrated vorticity causes the interface to develop into a mushroom-like shape with spirals of heavy fluid circling the centres of vorticity. From 4.0 to 5.5 ms the arms of the instability begin to exhibit a secondary instability as they rotate inward. The centres of vorticity become visible in the Mie scattering experiments as centripetal acceleration evacuates them of smoke. From 6.0 ms onward the spirals near the centres of vorticity begin to break down and strong mixing occurs. In the last few frames the

Parameter	Symbol	1.5 waves	2.5 waves	Units
Initial amplitude (pre-shock)	a_0^-	3.0–3.3	1.9–2.2	mm
Initial amplitude (post-shock)	a_0^+	2.0–2.8	1.5–1.9	mm
Wavenumber	k	0.1059	0.1765	mm^{-1}
Shock Mach number	M_s	1.2	1.2	None
Initial growth rate	$\dot{a}_0$	7.3–8.5	6.3–7.9	mm ms^{-1}
Piston velocity	V	62.51–63.82	65.92–70.45	mm ms^{-1}
Non-dimensional initial amp.	ka_0^+	0.21–0.30	0.26–0.34	None
Atwood number (post-shock)	A^+	0.68	0.68	None
Shaking frequency	f_{shake}	3.72	4.60	Hz
Shaking amplitude	a_{shake}	1.0	1.0	mm

TABLE 1. Parameters extracted from single-mode planar-laser-induced Mie scattering experiments for two different wavenumbers. Parameters f_{shake} and a_{shake} are imposed using a stepper motor controller and an eccentric cam. The superscripts $-$ and $+$ correspond to pre-shock and post-shock states respectively.

Parameter	Symbol	1.5 waves	2.5 waves	Units
Initial amplitude (pre-shock)	a_0^-	3.0	1.1	mm
Wavenumber	k	0.106	0.176	mm^{-1}
Shock Mach number	M_s	1.21	1.21	None
Piston velocity	V	63.5	63.5	mm ms^{-1}
Non-dimensional initial amp.	ka_0^-	0.32	0.12	None
Atwood number (post-shock)	A^+	0.66	0.66	None
Shaking frequency	f_{shake}	3.72	4.59	Hz
Shaking amplitude	a_{shake}	1.5	1.0	mm
Driver pressure	p_d	239.2	239.2	kPa

TABLE 2. Parameters extracted from single-mode particle image velocimetry experiments for two different wavenumbers. The superscripts $-$ and $+$ correspond to pre-shock and post-shock states respectively.

mushroom stems begin to thin, while turbulent diffusion causes the vorticity to spread into the surrounding flow. Table 1 contains parameters for the planar Mie scattering experiments and table 2 contains parameters for the PIV experiments. The interface velocity was extracted as the slope of a linear fit to the mean interface displacement versus time during the linear growth phase. The time at which this curve fit intersected the initial mean interface location (average of bubble and spike locations) was set to $t = 0$. The initial growth rate and amplitude were extracted using a linear fit to amplitude versus time plots during the linear growth phase.

We want to produce a single-mode perturbation, but it is likely that the method used to produce the initial perturbation will introduce higher harmonics on the interface. To examine the modal content of the initial perturbation, a discrete Fourier transform of an edge-detected image of the initial perturbation was constructed. Figure 6 shows the spectrum of the initial perturbation for a 1.5-wavelength and a 2.5-wavelength experiment. These spectra show strong peaks at the dominant wavenumbers, some weaker harmonics, and little spectral content for the highest wavenumbers. While the spectra are not completely single-mode, the large dimensionless amplitude ka for the dominant modes will cause them to quickly dominate the flow.

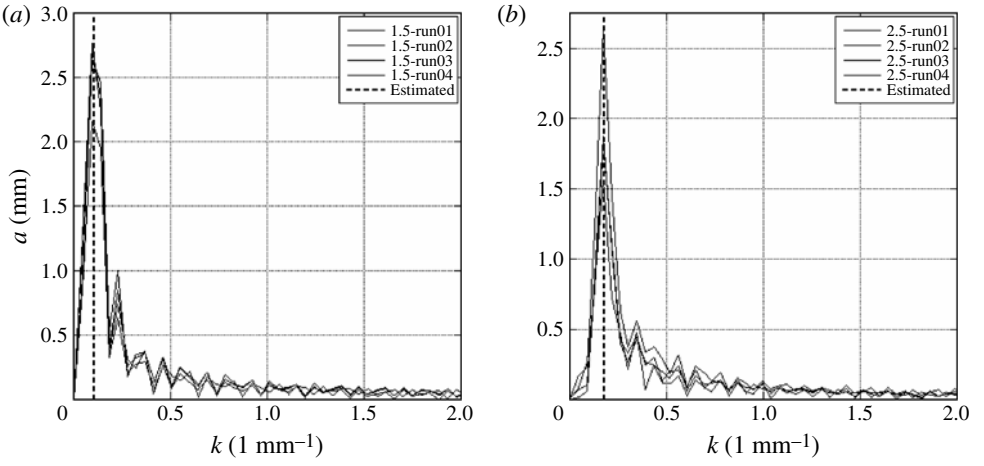

FIGURE 6. Spectra of wavenumbers present in the initial perturbation of Mie scattering experiments: (*a*) 1.5 wavelengths; (*b*) 2.5 wavelengths. Both sets of spectra exhibit weak higher harmonics and a strong peak near the desired wavenumber.

4.2. *Comparisons with simulations*

Several simulations were completed to compare with experiments. Figure 7 shows a comparison of experimental images with images from a Miranda simulation. Good qualitative agreement is observed throughout this sequence. Some slight differences are observable, with the experiment exhibiting less symmetry and finer detail. The secondary instability is observed to occur earlier in the experiment and also becomes more turbulent at later times. Also in the experiments, the vortex cores are marked by the evacuation of smoke particles caused by the strong centrifugal forces present in these regions.

Figure 8 compares experimental amplitude measurements to those extracted from a Miranda simulation and an Ares simulation. This comparison shows good qualitative agreement at early times. However, at later times, the amplitude of the simulations is noticeably less than that of the experiment. A comparable simulation was run using the Ares code which is also shown in figure 8. As observed in figure 8, the Ares and Miranda simulations produced similar amplitude trends. Note that the data of figure 8 are plotted in terms of the dimensionless variables $k\dot{a}_0 t$ versus $k(a - a_0)$ with $\dot{a}_0$ obtained from Richtmyer's theory. These variables are used in order for amplitude curves with different initial growth rates to have a slope of unity near the origin, and to better reveal differences in the nonlinear behaviour. This rescaling is shown to collapse the experimental amplitude measurements well into the nonlinear region (Jacobs & Krivets 2005). However, both simulations are observed to produce a non-dimensional late-time growth rate that is less than that produced by the experiment.

4.3. *Effects of additional acceleration*

The amplitude discrepancies observed in figure 8 can be explained by examining the late-time interface velocities. Figure 9 shows the velocity of the bubble tips in the laboratory fixed frame for four 2.5-wavelength experiments. Note that the bubble velocity should decay to zero as $t \to \infty$ in the reference frame moving with the mean interface location. This implies that bubbles should approach constant velocity in the laboratory frame. In our experiments, however, the bubble velocities are observed to

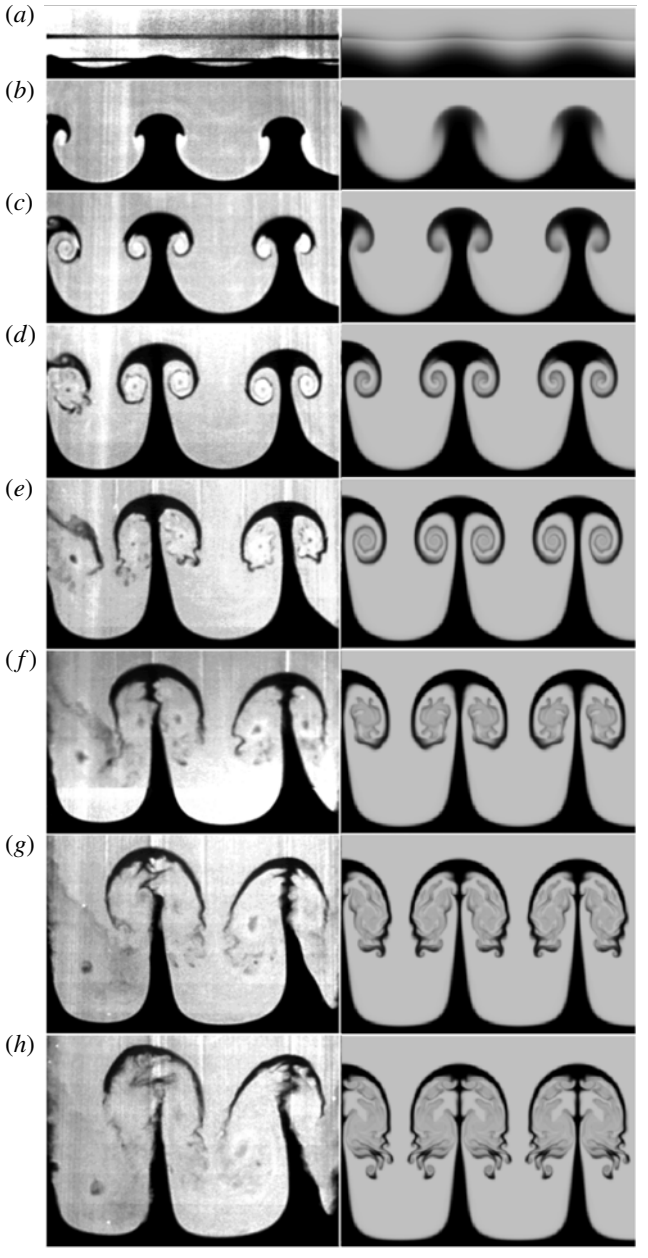

FIGURE 7. Montage of (*a*) experimental images compared with (*b*) pseudocolour images of species mass fraction from a Miranda simulation at (*a*) $t = -0.08$ ms, (*b*) $t = 1.42$ ms, (*c*) $t = 2.92$ ms, (*d*) $t = 4.42$ ms, (*e*) $t = 5.92$ ms, (*f*) $t = 7.42$ ms, (*g*) $t = 8.92$ ms, and (*h*) $t = 10.42$ ms. Good qualitative agreement is observed, but an amplitude discrepancy is present.

be increasing with time at late times. In order to investigate this further, several flat interface experiments were undertaken in which no initial perturbation was imposed. Figure 10 shows interface velocity measurements taken from four of these experiments.

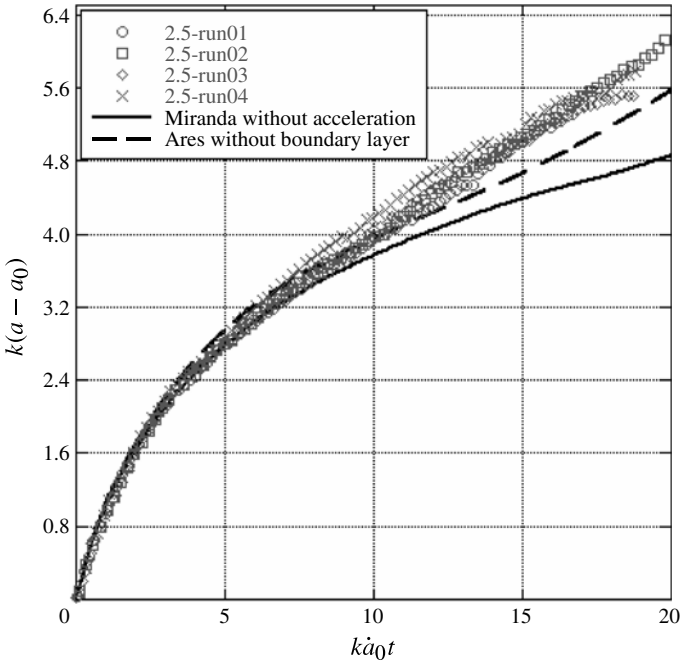

FIGURE 8. Non-dimensional amplitude for two simulations compared with 2.5-wavelength experimental data. The simulations without boundary layers or acceleration have lower amplitudes than the experiments.

As can be seen in the plots, the velocity increases with time, indicating acceleration. Since the acceleration is directed from the light fluid into the heavy fluid, one would expect the addition of Rayleigh–Taylor instability to induce Richtmyer–Meshkov growth rates that are larger than those with no acceleration present. This additional Rayleigh–Taylor growth could explain the discrepancy observed in figure 8.

In one-dimensional gas dynamics theory, flat fluid interfaces with a shock wave impacting them from the light gas to the heavy gas are expected to reflect a shock or compression wave and transmit a shock or compression wave. The interface then moves at the constant velocity induced by the transmitted wave. Figure 10 shows a horizontal line indicating the expected results from a one-dimensional analysis. The figure shows that when accelerated by a shock wave, the interface travels at a speed initially less than that predicted by gas dynamics and then slowly accelerates, approaching but not reaching the one-dimensional result. In an attempt to understand this variation, two possible causes were investigated using numerical simulations. The first is the effect of the slots, the two 6 mm openings in the shock tube walls, on the resulting interface velocity. This effect was simulated in Miranda by applying a localized mixed boundary condition which allows the pressure to relax to the ambient value for the 0.75 cm of shock tube wall occupied by the slots. In figure 10 this simulation shows the shock interaction to accelerate the interface to a constant velocity lower than the theoretical value. Thus, the slots appear to reduce the impulsive acceleration of the interface, but do not produce acceleration.

The other possible cause for the acceleration that was investigated in the simulations was the effect of the boundary layers that are known to grow on the shock tube

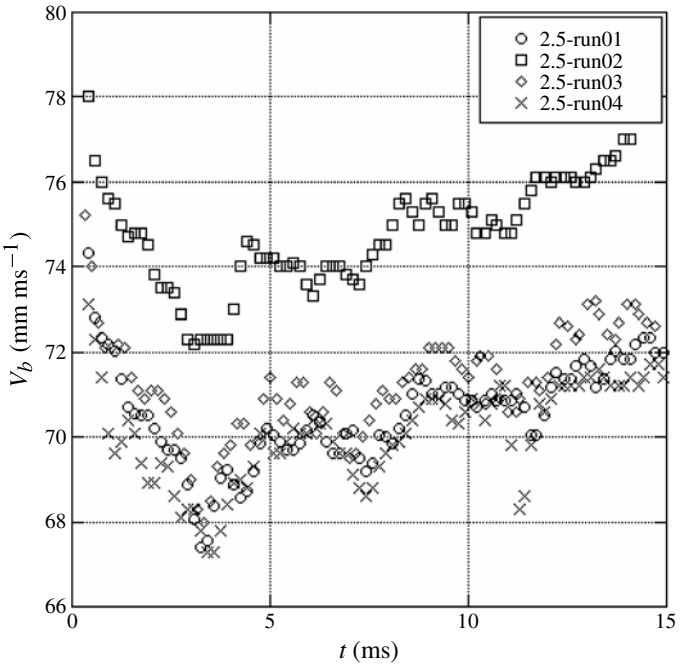

FIGURE 9. A plot of the bubble velocities relative to the shock tube fixed frame from four experiments showing how they accelerate at late times, in disagreement with most predictions. The flat interfaces in the experiment experience a similar acceleration to that experienced by the bubbles.

wall following shock acceleration. Contact surface acceleration was described by Glass & Patterson (1955) when they observed the velocity of the contact surfaces in their experiments increasing with the distance traversed by the contact surface. This effect has more recently been produced in the numerical simulations of Badcock (1992). The theory developed by Roshko (1960) for laminar boundary layers and Brocher (1964) for turbulent boundary layers describes the acceleration as being caused by mass leakage through the interface caused by the boundary layer. In order to conserve mass in a shock fixed reference frame, the length of the gas column between the interface and the shock must decrease. According to Mirels (1956), boundary layers will produce a wall-normal velocity which will act on the inviscid mean flow as a mass source or sink. For negative wall velocities, the mass sink will cause the generation of expansion waves that will accelerate the interface (Mirels & Braun 1957). These situations are assumed to be analogous to the boundary layer growing between the transmitted shock and the interface.

The theory as outlined in Brocher (1964) consists of balancing the flow entering through the shock with the flow leaking out of the interface and relating this to the change in volume of the column of gas. This leads to the following expressions relating non-dimensional gas column length to non-dimensional time:

$$\ln\left(\frac{1}{1-L^{1/2}}\right)+L^{1/2}=-\frac{T}{2} \tag{4.1}$$

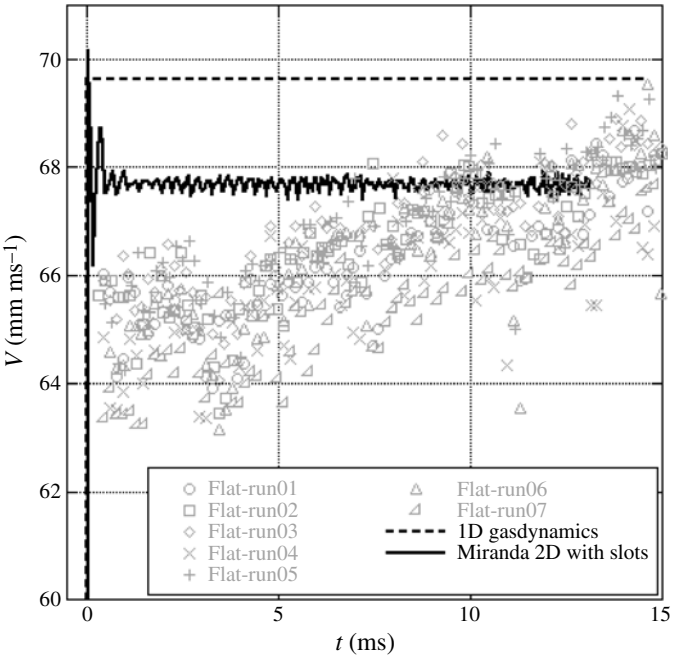

FIGURE 10. Comparison of results from flat interface experiments and a simulation in Miranda where the effects of the slots are approximately modelled.

for laminar boundary layers, and

$$\frac{1}{4}\ln\left(\frac{1+L^{1/5}}{1-L^{1/5}}\right)+\frac{1}{2}\tan^{-1}(L^{1/5})-L^{1/5}=\frac{T}{5} \tag{4.2}$$

for turbulent boundary layers. The non-dimensional length is $L=l/l_m$, where l and l_m are the physical length and maximum length of the gas column, respectively, where

$$l_m=\left(\frac{d}{4\beta}\right)^2\left(\frac{\rho_2}{\rho_w}\right)^2\frac{(u_t-u_2)^2}{u_2}\left(\frac{\rho_2}{\mu_w}\right), \tag{4.3}$$

and for turbulent boundary layers

$$l_m=\left(\frac{u_t}{u_2}\right)\left(\frac{d}{4\beta}\right)^{5/4}\left(\frac{\rho_w u_t}{\nu_w}\right)^{1/4}. \tag{4.4}$$

Here d is the width of the shock tube, the subscript w indicates wall values, the subscript 2 denotes shocked test gas values, ν is the kinematic viscosity, and β is an empirical boundary layer scaling. The non-dimensional time scale is $T=(u_t-u_2)t/l_m$, where u_t is the velocity of the transmitted shock and u_2 is the velocity induced by the transmitted shock. For the Mirels & Braun (1957) approximation, all terms relating to the regions above the interface are ignored and the weak shock limit is assumed. This

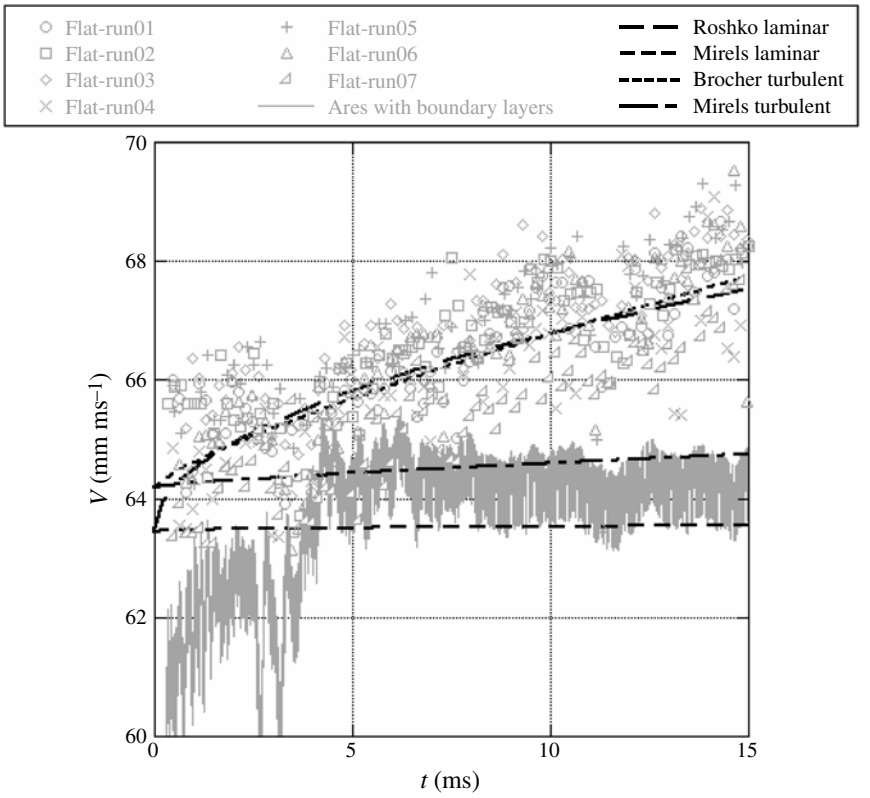

FIGURE 11. Comparison of results from flat interface experiments, a simulation in Ares where the effects of boundary layers are approximately modelled, the boundary layer leakage models of Roshko (1960) and Brocher (1964), and the compressible one-dimensional wave generation models of Mirels & Braun (1957).

leaves the expression

$$\frac{\Delta u_2}{a_2}\left(\frac{d}{u_t}\right)^{1-n}\left(\frac{a_2 d}{\nu_2}\right)^{n}\frac{1-n}{2L_2\,(M_2^2)^{1-n}}=\frac{4}{(\gamma+1)M_2}\times\left[\left(1+\frac{(\gamma+1)M_2}{8}\right)\left(\frac{1-\dfrac{u_2}{u_t}}{1-\dfrac{\gamma+1}{4}M_2}\right)^{1-n}-\left(1+\frac{\gamma+1}{4}M_2-\frac{u_2}{u_t}\right)^{1-n}\right]t^{1-n},\tag{4.5}$$

for the velocity perturbation Δu_2 at the interface. Here $n=1/2$ for laminar, $n=1/5$ for turbulent, and the parameter L_2 is given in Mirels (1956) by equation (D3c) for laminar and (E1c) for turbulent. The parameters a_2, M_2 and γ are the sound speed, the Mach number, and the adiabatic index of the shocked test gas respectively.

Figure 11 shows the behaviours of the various acceleration models. The transmitted Mach number and the boundary layer β parameter were adjusted iteratively to produce the best agreement with the data for the Roshko (1960) and Brocher (1964) models. It can be seen that for the laminar case, this produces a somewhat large β parameter. In this case $\beta^2=47$, which is much larger than the theoretical value for incompressible

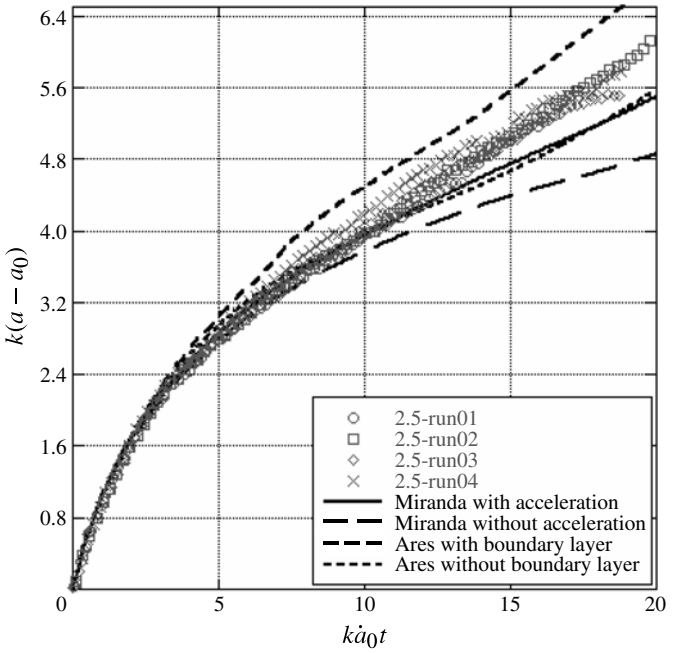

FIGURE 12. Non-dimensional amplitude for four simulations compared to data. The simulations without boundary layers have lower amplitudes than the experiments. The simulations with boundary layers and acceleration exhibit increased amplitudes and growth rates agreeing better with experimental trends.

laminar flow of $\beta^2 = 2.962$ (Schlichting & Gersten 2000). However, a very realizable transmitted Mach number, $M_t = 1.276$, is found. For the turbulent case $\beta^2 = 0.0021$, which is very close to the theoretical value of $\beta^2 = 0.0023$ based on incompressible, turbulent flow, with a 1/7 power velocity profile (von Kármán 1921). In this case $M_t = 1.28$, which is reasonable compared to a theoretical value of $M_t = 1.27$ for an incident shock strength of $M_s = 1.18$ (as was found by matching interface velocity in a Miranda simulation to experiments). It is notable that the turbulent model of Brocher (1964) approaches an acceleration of around 200 m s^{-2} at late times. The model of Mirels & Braun (1957) produces worse agreement as it lacks a free parameter. It does consider compressibility effects and shock attenuation which would tend to decrease the acceleration of the interface. It is important to remember that these models were developed to predict the arrival time of the contact surface. However, the agreement of the Brocher (1964) model indicates that a turbulent boundary layer may produce the acceleration observed in the experiments.

Boundary layers were produced in the Ares simulations applying no-slip boundary conditions on the walls. This produced thick, laminar, two-dimensional and under-resolved boundary layers which is in contrast to the turbulent three-dimensional boundary layers likely to be present in the experiments. It can be observed in figure 11 that these boundary layers produce a prolonged accelerative effect on the interface. The magnitude of this acceleration is of the order of that observed in the flat interface experiments, and using linear fits to the data, the magnitude of this acceleration is found to be approximately 200 m s^{-2}.

Figure 12 shows experimental amplitudes compared to amplitudes from Ares simulations and Miranda simulations with accelerative effects present. Simulations

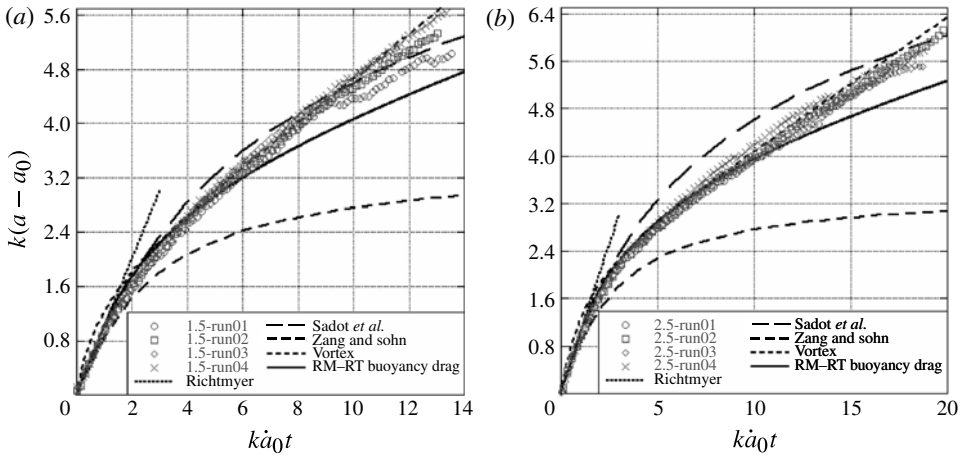

FIGURE 13. Amplitude measurements from Mie scattering experiments in non-dimensional coordinates compared to models for the Richtmyer–Meshkov instability: (*a*) 1.5 wavelengths; (*b*) 2.5 wavelengths. The RM–RT buoyancy–drag model plotted here uses Rayleigh–Taylor instability theory to attempt to account for accelerations present in the shock tube experiments.

were run using Ares to determine how boundary layers might affect the late-time growth rates. As shown in figure 12, the presence of boundary layers produces increased late-time amplitudes and growth rates. The agreement with experimental data seen in figure 12 is better than should be expected, as this simulation is two-dimensional and does not simulate the boundary layers properly. Richtmyer–Meshkov (RM) instability with an imposed Rayleigh–Taylor (RT) instability was also simulated in Miranda by imposing a gravitational acceleration of 200 m s^{-2} at $t = 1$ ms in order to simulate the acceleration measured in flat interface experiments. This produced an increased late-time growth rate consistent with that observed in the experiments as shown in figure 12. In addition, the simulations also produced a constant late-time growth rate also observed in the experiments. Nevertheless, the magnitude of the late-time growth rate differs slightly from that measured.

It should be noted that there are other effects not accounted for in our two-dimensional simulations that could cause the discrepancies observed in the comparisons of the experiments and simulations. For example three-dimensionality could cause this difference. In order to investigate this possibility, preliminary three-dimensional simulations using plausible guesses for initial conditions in the spanwise direction in the form of noise were performed. However, these simulations failed to produce the large differences in growth observed when boundary layers are added. It is possible that there is some other type of three-dimensional disturbance (most probably a long-wavelength one) causing this difference. However, in the absence of knowing the precise form of this perturbation we are unable to carry out this study at this time. We must therefore reserve it for future study.

4.4. *Comparison with models*

Figures 13 and 14 show comparisons of experimental amplitude and growth rate measurements with those predicted by the linear early-time model of Richtmyer (1960), along with the nonlinear models described below.

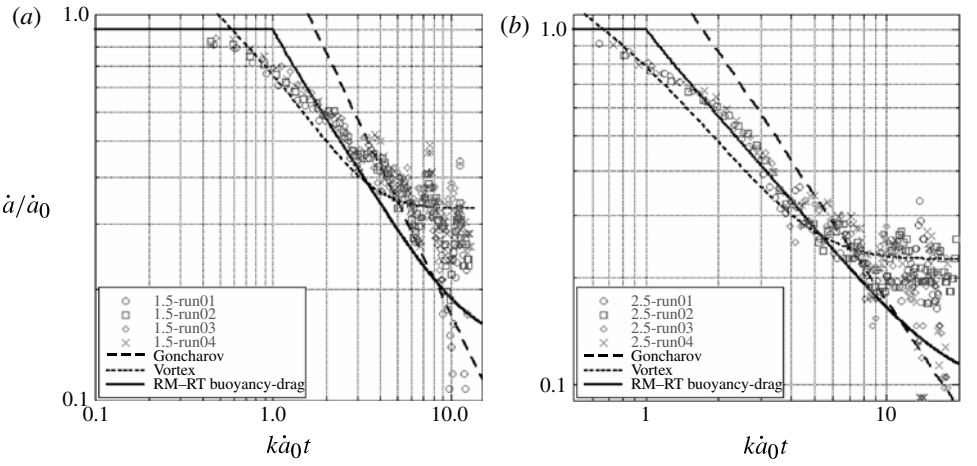

FIGURE 14. Measured growth rates from Mie scattering experiments compared to the Goncharov model, the vortex model, and the combined RM–RT buoyancy–drag model: (*a*) 1.5 wavelengths; (*b*) 2.5 wavelengths.

4.4.1. *The Zhang and Sohn model*

Zhang & Sohn (1997*b*) modelled the nonlinear growth of the RM instability using Padé approximates in which the growth rate can be expressed as

$$\dot{a}_{b/s} = \dot{\eta}_{even} \mp \dot{\eta}_{odd}, \tag{4.6}$$

where the upper sign is for the bubble and the lower sign is for the spike,

$$\dot{\eta}_{odd} = \frac{\dot{a}_0}{1 + a_0\dot{a}_0k^2t + \max\{0, a_0^2k^2 - A^2 + 1/2\}\dot{a}_0^2k^2t}, \tag{4.7}$$

and

$$\dot{\eta}_{even} = \frac{Ak\dot{a}_0^2t}{1 + 2k^2a_0\dot{a}_0t + 4k^2\dot{a}_0^2[a_0^2k^2 + (1/3)(1 - A^2)]t^2}, \tag{4.8}$$

where $\dot{a}_0 = kA\Delta Va_0$ according to the theory of Richtmyer (1960). The Zhang and Sohn model produces the worst agreement with our experiments due to its $1/t^2$ late-time growth behaviour.

4.4.2. *The Sadot et al. model*

The model of Sadot *et al.* (1998) is an empirical model with parameters chosen to match observed asymptotic behaviours of the Richtmyer–Meshkov instability. In this model the growth rate is expressed as

$$\dot{a}(t) = \dot{a}_0\frac{1 + \dot{a}_0kt}{1 + (1 \pm A)\dot{a}_0kt + \dfrac{1}{2\pi C}\left(\dfrac{1 \pm A}{1 + A}\right)\dot{a}_0^2k^2t^2}, \tag{4.9}$$

with the remaining parameter chosen as $C = 1/(3\pi)$ for $A \gtrsim 0.5$. The model parameters are chosen to produce good agreement at late times with experiments, simulations, and with the early-time behaviour as given by the first two terms of the asymptotic expansion of Zhang & Sohn (1997*a*). Expanding (4.9) around $t \to \infty$ leads

to the late-time behaviour of

$$\dot{a}_{b/s} \rightarrow \frac{1}{\dfrac{1}{2\pi C}\left(\dfrac{1 \pm A}{1 + A}\right) kt}. \tag{4.10}$$

Comparing the Zhang and Sohn and the Sadot models to the data in figure 13 shows that the Sadot model provides significantly better agreement with the data than does the Zhang and Sohn model, a finding also observed in previous experiments (Jacobs & Krivets 2005). However, contrary to what was observed in the earlier experiments, the Sadot model appears to diverge from the data at the latest times. It should be noted that the experiments of Jacobs & Krivets (2005) used a technique that allows the acquisition of only one image per experiment, thus introducing scatter to the data. It can be seen in figure 13 that the Sadot *et al.* (1998) model passes through the data but the trajectories at late times are different. Thus this late-time trend could have easily been obscured by the data scatter. Since the Sadot *et al.* (1998) model is based on providing good agreement with experimental data, it may be influenced due to the presence of shock tube boundary layers in their experiments, and thus may not accurately represent the boundary-layer-free situation one might expect to find in a shock tube with much larger cross-sectional area.

4.4.3. *The buoyancy–drag model*

Starting from a kinematic viewpoint, the Richtmyer–Meshkov instability can be modelled as a series of bubbles of fluid either rising or falling while surrounded by a heavier or lighter fluid (Oron *et al.* 2001). The equations of motion for the bubble and spike are

$$(\rho_2 + C_a\rho_1)\ddot{a} = g_{eff}(\rho_2 - \rho_1) - \frac{C_d}{\lambda}\rho_1 (\dot{a})^2, \tag{4.11}$$

and

$$(\rho_1 + C_a\rho_2)\ddot{a} = g_{eff}(\rho_2 - \rho_1) - \frac{C_d}{\lambda}\rho_2 (\dot{a})^2, \tag{4.12}$$

where C_a is the virtual mass coefficient, C_d is a drag coefficient, and λ is the wavelength of the instability. This results in

$$\ddot{a} = gC - B\dot{a}^2, \tag{4.13}$$

with the constants gC and B expressed as

$$gC_{b/s} = \frac{2gA}{1 \mp A + C_a(1 \pm A)} \tag{4.14}$$

and

$$B_{b/s} = \frac{C_d(1 \pm A)}{\lambda[1 \mp A + C_a(1 \pm A)]}. \tag{4.15}$$

For Richtmyer–Meshkov instability, $g_{eff} \rightarrow 0$, and Oron *et al.* (2001) chose $C_a = 2$ and $C_d = 6\pi$ (for two dimensions) resulting in

$$\dot{a}^2_{b/s} = -\frac{3 \pm A}{3k(1 \pm A)}\ddot{a}_{b/s}. \tag{4.16}$$

The growth rates can be found by integrating (4.16), resulting in

$$\dot{a}_{b/s} = \frac{3 \pm A}{3k(1 \pm A)} \frac{1}{kt}. \tag{4.17}$$

It can be seen that (4.17) exhibits a $1/t$ late-time dependence and matches what Goncharov (2002) found using a method similar to Layzer (1955). Figure 14 shows the experimentally measured growth rates plotted in logarithmic form. Thus a $1/t$ late-time dependence will be given by a straight line with a -1 slope in these plots. Also shown in figure 14 are lines indicating the asymptotic behaviour given by (4.17), which appears to agree with the data at intermediate times but is unable to properly predict the trends in the data at early and late times.

4.4.4. *The RM–RT buoyancy–drag model*

One could argue that the discrepancy with the nonlinear models might be anticipated because of the observed late-time acceleration present in the experiments, and thus it might be expected that better agreement could be obtained by properly accounting for the accelerations present in the shock tube experiments. The differential equation found for the buoyancy–drag model is known to reliably predict single-mode late-time Rayleigh–Taylor growth as well as that of Richtmyer–Meshkov instability. If it is assumed that the difference in growth rate between the simulation and experiment is caused by the addition of a nearly constant acceleration, one would expect that the buoyancy–drag model could be applied by retaining both terms on the right-hand side of (4.13). Furthermore, it is reasonable to expect the initial growth rate to be well modelled by Richtmyer–Meshkov linear stability theory. Thus, we will model the experiments by imposing a constant acceleration after the initial linear Richtmyer–Meshkov instability stage, matching the linear Richtmyer–Meshkov instability amplitude to a nonlinear single-mode Rayleigh–Taylor instability amplitude at $k\dot{a}_0 t = 1$. Thus,

$$\dot{a} = \dot{a}_0 = kAVa_0 \tag{4.18}$$

for $k\dot{a}_0 t \leqslant 1$, and

$$\dot{a} = \sqrt{\frac{gC}{B}} \coth[\sqrt{gCB}(t + C_R)] \tag{4.19}$$

for $k\dot{a}_0 t > 1$, with

$$C_R = \frac{1}{\sqrt{gCB}} \coth^{-1}\left[\dot{a}_0 \sqrt{\frac{B}{gC}}\right] - \frac{1}{k\dot{a}_0}. \tag{4.20}$$

The result of this RM–RT modified buoyancy–drag model, using an acceleration of approximately 200 m s^{-2}, is shown in figures 13 and 14. As can be seen, this model agrees well with the data at early times through the nonlinear transition, but fails to properly capture the late-time growth rate of the instability (see figure 14).

4.4.5. *The Likhachev and Jacobs vortex model*

As shown by Jacobs & Sheeley (1996), the two-dimensional fluid motion induced by the Richtmyer–Meshkov instability can be described by two rows of equally spaced positive and negative line vortices. This model was extended by Sohn (2011) to viscous instability for $A \to 0$. The vortex model of Likhachev & Jacobs (2005) extends the model of Jacobs & Sheeley (1996) to systems with non-zero Atwood numbers. The model attempts to capture the asymmetry-causing effects of the Atwood number by

introducing a perturbative displacement ϵ to the vortex spacings. In this model, the streamfunction takes the form

$$\Psi = \frac{\Gamma}{4\pi} \ln \left(\frac{\cosh(ky) + \cos[k(x+\epsilon)]}{\cosh(ky) - \cos[k(x-\epsilon)]} \right), \tag{4.21}$$

where the vortices are displaced by $\pm\epsilon$ from the uniform spacing. The most significant difference between the two models is that the perturbed vortex row moves upward as a whole in the direction of the light fluid with the constant velocity

$$V = \frac{k\Gamma}{4\pi} \tan(k\epsilon). \tag{4.22}$$

This velocity can be subtracted from the total velocity in order to determine the bubble and spike growth rates in the reference frame travelling with the vortex system. The bubble and spike growth rates are given by

$$\frac{\mathrm{d}(ka_{b/s})}{\mathrm{d}\tau} = \mp \frac{\cos(k\epsilon)}{\cosh(ka_{b/s}) \pm \sin(k\epsilon)} - \frac{1}{2} \tan(k\epsilon), \tag{4.23}$$

where the non-dimensional time is defined as $\tau = k^2\Gamma t/(2\pi)$. This implies that the growth rate of the full (bubble-to-spike) amplitude of the instability will approach constant value at late times. In viewing figure 12, the experimental data indeed appear to asymptote to a constant growth rate in agreement with what is predicted by the vortex model, and does not appear to have the $1/t$ dependence predicted by most Richtmyer–Meshkov models. The weakness of this model, however, lies in the fact that the circulation and vortex spacing are unknown. Nevertheless, they can be used as fitting parameters, adjusted to obtain the best agreement with the experimental data. Figures 13 and 14 show plots of the vortex model with parameters chosen to provide the best fit. As can be seen in this plot, the vortex model seems to capture the character of the instability throughout the largest portion of the development. This is in part due to the parameters being adjusted to produce the best agreement. Nevertheless, the vortex model does have the proper asymptotic behaviour, implying that point vortices do well to model the flow.

4.5. *Circulation comparisons*

Figure 15 shows non-dimensional circulation extracted from the PIV experiments compared with that obtained from four simulations including Ares with and without boundary layers and Miranda with and without acceleration. In this case the circulation was obtained by integrating the vorticity over one half-wavelength using

$$\Gamma = \int \int_{\lambda/2} \omega_z \, \mathrm{d}x \, \mathrm{d}y. \tag{4.24}$$

Circulation is an important parameter governing the growth of the instability; as shown by Jacobs & Sheeley (1996) the initial growth rate is proportional to the magnitude of the circulation deposited by the shock. As shown in figure 15, plotting the non-dimensional group based on the circulation estimate $\Gamma = 4\dot{a}_0/k$ of Jacobs & Sheeley (1996) effectively collapses the data from the two simulations computed without the effects of boundary layers or acceleration. The circulation extracted from the PIV experiments is observed to grow with time. Similar trends are also observed in the numerical simulations without acceleration or boundary layers present, but to a lesser degree. The numerical simulations with the effects of boundary layers

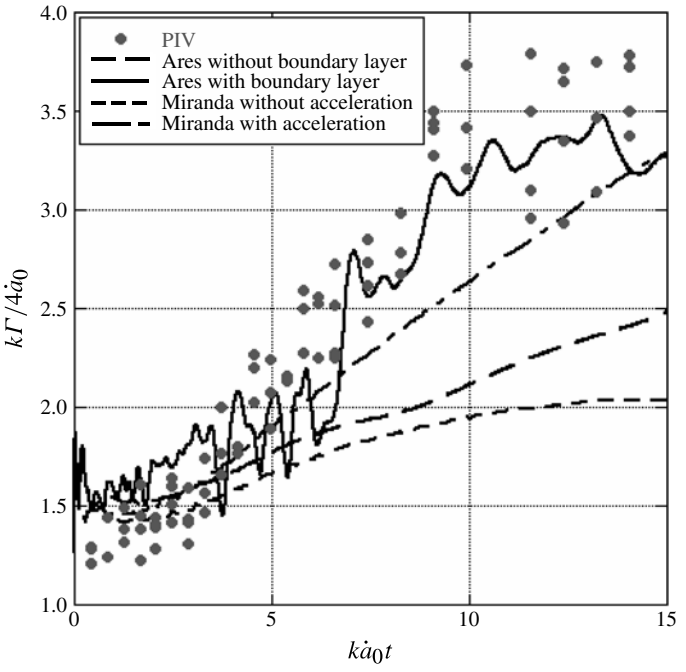

FIGURE 15. Circulation from four simulations compared with PIV data from a 2.5-wavelength experiment. The non-dimensionalization is based on the theory of Jacobs & Sheeley (1996) and causes the circulation from the two simulations without boundary layers or acceleration to nearly collapse. The boundary layers cause an increase in circulation compared to the other simulations. The simulation with acceleration sees a continuous increase in circulation.

and acceleration included exhibit a larger increase in circulation in better agreement with the data at early times. The Miranda simulation with acceleration begins to diverge from the data at late times while the Ares simulation follows the data. This agreement, however, may be caused by the distortion of the interface, resulting in vorticity leaving the rectangular interrogation window. One possible explanation for the early-time increase in circulation is Rayleigh–Taylor-induced vorticity production caused by interfacial acceleration. This increase in circulation is also observed in the Miranda simulations with acceleration, as vorticity is continually produced by RT growth. Additional circulation is produced by baroclinic generation and can be seen in Miranda simulations without acceleration.

To characterize the vortex model, the two parameters extracted from fitting the model to the data, the circulation (Γ) and the vortex displacement (ϵ) are compared to PIV experiments in figure 16. Using the distance between the centres of vorticity in PIV experiments, an experimental ϵ value can be found and compared to that extracted from the vortex model. As shown in figure 16, the measured vortex displacement initially increases with time and then slowly decreases during the experiment. The extracted value of vortex displacement, $\epsilon = 3.0$ mm, is very close to the mean value of the displacement over the entire experiment. The PIV experiments show the circulation growing from around the Jacobs & Sheeley (1996) value of circulation based on linear stability theory ($\Gamma = 0.16$ m s^{-2}) up to approximately the value found from fitting the

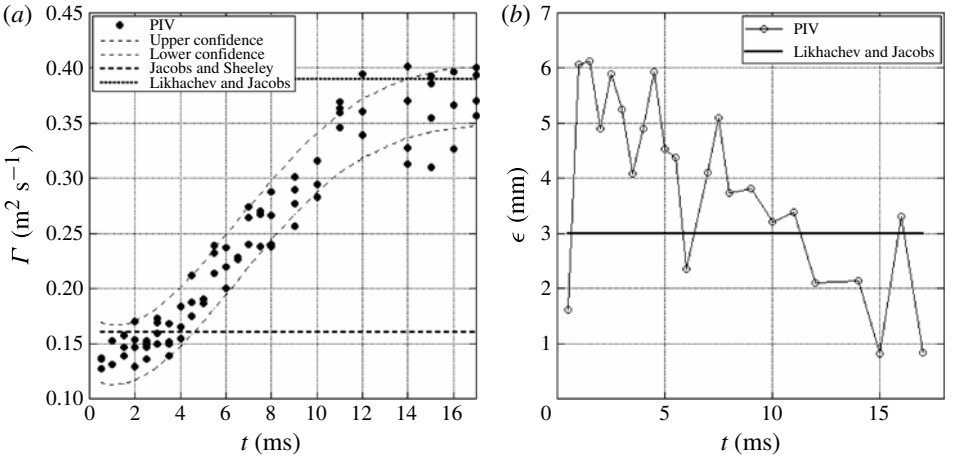

FIGURE 16. (*a*) Circulation developed in the PIV experiments compared with the extracted value of circulation from the Likhachev & Jacobs (2005) vortex model. The extracted value is very close to the peak value of the measured circulation. The Jacobs & Sheeley (1996) value predicts the initial vorticity. (*b*) The separations of the centres of vorticity compared to the spacing extracted from the vortex model.

model to the data ($\Gamma = 0.39$ m s^{-2}). Thus the asymptotic circulation value agrees well with the estimated circulation value of the vortex model.

5. Conclusions

Experiments were performed to study the late-time growth of the Richtmyer–Meshkov instability from a diffuse nearly sinusoidal initial perturbation into a fully turbulent flow. This experiment is an improvement over previous experiments because it enables us to record time sequences of the instability from known membraneless initial perturbations out to previously unattainable late times. The 2.0 m length of the test section makes this study the longest-duration single-mode Richtmyer–Meshkov experiment to date. This long duration allows the observation of the growth of the instability into the nonlinear region and the beginning of turbulence. The experiments used Mie scattering to extract amplitude and growth rates while PIV experiments were used to extract vorticity and circulation. Experimental images exhibit the growth of mushroom structures until the point where secondary instability and turbulent diffusion cause them to break down. Extracting the time series of the instability represents an improvement over previous experiments, which were only able to acquire one image per experiment.

Experimental measurements are compared to those obtained from numerical simulations, which are unable to capture all of the physical effects found in the shock tube such as slots and boundary layers. It is shown that the slots in the shock tube reduce the impulse imparted to the interface, while the boundary layers produce prolonged accelerative effects. Attempts were made to model the acceleration using previously published shock tube boundary layer analyses. The turbulent boundary layer theory of Brocher (1964) produces the best agreement with measurements of the flat interface acceleration. This indicates that the accelerative phenomenon may best be described by a leak at the interface caused by the growth of turbulent

boundary layers. The acceleration present in the shock tube causes disagreement with existing Richtmyer–Meshkov instability models and simulations due to the presence of Rayleigh–Taylor instability. Introducing acceleration to the numerical simulations yields improved agreement with late-time growth rate and amplitude trends. Numerical simulations with boundary layers present also improve agreement and exhibit increased late-time growth rates. Since boundary layers are no doubt present in all RM experiments using shock tubes of this size, this result implies that empirical models evaluated using shock tube experiments such as the model of Sadot *et al.* (1998) may be influenced by the presence of acceleration. The presence of acceleration also produces increased circulation when modelled in simulations, improving the agreement between simulations and experiments. The Likhachev & Jacobs (2005) vortex growth model, when fitted to experiments, produces a circulation estimate that agrees well with the asymptotic value found using PIV measurements.

Due to the very late times observed, the present experiments make a good basis for comparison with late-time Richtmyer–Meshkov models. The amplitude of the instability is modelled well by most models at early times, but the model of Zhang & Sohn (1997*b*) exhibits the worst agreement at late times. The model of Sadot *et al.* (1998) exhibits improved agreement but appears to have a different functional dependence than the experiments at late times. Agreement with the models can be improved by accounting for acceleration. This is done using the RM–RT buoyancy–drag model, which exhibits an increased constant late-time growth rate which agrees better with experiments. The Goncharov (2002) model agrees at intermediate times but fails at the latest experimental times. The growth rate of the instability is approximated best by the Likhachev & Jacobs (2005) vortex model. The agreement with the vortex model implies that the vorticity distributions present in the experiment resemble the perturbed point vortices of the model. The vortex model, however, has the shortcoming that it is impossible to determine the parameters from the initial perturbation of the instability as the parameters can only be determined using a curve fit to the experimental data.

Acknowledgements

This research is supported by Lawrence Livermore National Laboratory and by the US Department of Energy National Nuclear Security Administration under its Stewardship Science Academic Alliance Program. Lawrence Livermore National Laboratory is operated by Lawrence Livermore National Security, LLC, for the US Department of Energy, National Nuclear Security Administration under Contract DE-AC52-07NA27344. The authors would also like to acknowledge the help and contributions of Dr A. Cook for his expertise with the Miranda code, Dr P. Miller for his helpful discussions, and Dr V. Krivets for his experience and practical knowledge of the shock tube used for these experiments.

REFERENCES

ABRAMOWITZ, M. & STEGUN, I. A. 1964 *Handbook of Mathematical Functions with Formulas, Graphs, and Mathematical Tables*. National Bureau of Standards Applied Mathematics Series.

AURE, R. & JACOBS, J. W 2008 Particle image velocimetry study of the shock-induced single mode Richtmyer–Meshkov instability. *Shock Waves* **18**, 161–167.

BADCOCK, K. J. 1992 A numerical simulation of boundary layer effects in a shock tube. *Intl J. Numer. Meth. Fluids* **14**, 1151–1171.

BALAKUMAR, B. J., ORLICZ, G. C., TOMKINS, C. D. & PRESTRIDGE, K. P. 2008 Dependence of growth patterns and mixing width on initial conditions in Richtmyer–Meshkov unstable fluid layers. *Phys. Scr.* **T123**, 014013.

BENJAMIN, R. F., TREASE, H. E. & SHANER, J. W. 1984 Coherent density gradients in water compressed by a modulated shock wave. *Phys. Fluids* **27**, 2390–2393.

BONAZZA, R. & STURTEVANT, B. 1996 X-ray measurements of growth rates at a gas interface accelerated by shock waves. *Phys. Fluids* **8**, 2496–2512.

BROCHER, E. F. 1964 Hot flow length and testing time in real shock tube flow. *Phys. Fluids* **7**, 347–351.

COLLINS, B. D. & JACOBS, J. W. 2002 PLIF flow visualization and measurements of the Richtmyer–Meshkov instability of an air/SF_6 interface. *J. Fluid Mech.* **464**, 113–136.

COOK, A. W. 2007 Artificial fluid properties for large-eddy simulation of compressible turbulent mixing. *Phys. Fluids* **19**, 055103.

COOK, A. W. & CABOT, W. H. 2004 A high-wavenumber viscosity for high-resolution numerical methods. *J. Comput. Phys.* **195**, 594–601.

COOK, A. W. & CABOT, W. H. 2005 Hyperviscosity for shock–turbulence interactions. *J. Comput. Phys.* **203**, 379–385.

DIMONTE, G. & RAMAPRABHU, P. 2010 Simulations and model of the nonlinear Richtmyer–Meshkov instability. *Phys. Fluids* **22**, 4014104.

EDWARDS, M. J., LINDL, J. D., SPEARS, B. K., WEBER, S. V., ATHERTON, L. J., BLEUEL, D. L., BRADLEY, D. K., CALLAHAN, D. A., CERJAN, C. J., CLARK, D., COLLINS, G. W., FAIR, J. E., FORTNER, R. J., GLENZER, S. H., HAAN, S. W., HAMMEL, B. A., HAMZA, A. V., HATCHETT, S. P., IZUMI, N., JACOBY, B., JONES, O. S., KOCH, J. A., KOZIOZIEMSKI, B. J., LANDEN, O. L., LERCHE, R., MACGOWAN, B. J., MACKINNON, A. J., MAPOLES, E. R., MARINAK, M. M., MORAN, M., MOSES, E. I., MUNRO, D. H., SCHNEIDER, D. H., SEPKE, S. M., SHAUGHNESSY, D. A., SPRINGER, P. T., TOMMASINI, R., BERNSTEIN, L., STOEFFL, W., BETTI, R., BOEHLY, T. R., SANGSTER, T. C., GLEBOV, V. Y., MCKENTY, P. W., REGAN, S. P., EDGELL, D. H., KNAUER, J. P., STOECKL, C., HARDING, D. R., BATHA, S., GRIM, G., HERRMANN, H. W., KYRALA, G., WILKE, M., WILSON, D. C., FRENJE, J., PETRASSO, R., MORENO, K., HUANG, H., CHEN, K. C., GIRALDEZ, E., KILKENNY, J. D., MAULDIN, M., HEIN, N., HOPPE, M., NIKROO, A. & LEEPER, R. J. 2011 The experimental plan for cryogenic layered target implosions on the national ignition facility: the inertial confinement approach to fusion. *Phys. Plasmas* **18** (5), 051003.

GLASS, I. I. & PATTERSON, G. N. 1955 A theoretical and experimental study of shock-tube flows. *J. Aero. Sci.* **22**, 73–100.

GONCHAROV, V. N. 2002 Analytical model of nonlinear, single-mode, classical Rayleigh–Taylor instability at arbitrary Atwood numbers. *Phys. Rev. Lett.* **88**, 134502.

GRINSTEIN, F. F., GOWHARDHAN, A. A. & WACHTOR, A. J. 2011 Simulations of Richtmyer–Meshkov instabilities in planar shock-tube experiments. *Phys. Fluids* **23**, 034106.

HAHN, M., DRIKAKIS, D., YOUNGS, D. L. & WILLIAMS, R. J. R. 2011 Richtmyer–Meshkov turbulent mixing arising from an inclined material interface with realistic surface perturbations and reshocked flow. *Phys. Fluids* **23**, 046101.

HERRMANN, M., MOIN, P. & ABARZHI, S. I. 2008 Nonlinear evolution of the Richtmyer–Meshkov instability. *J. Fluid Mech.* **612**, 311–338.

HOLMES, R. L., DIMONTE, G., FRYXELL, B., GITTINGS, M. L., GROVE, J. W., SCHNEIDER, M., SHARP, D. H., VELIKOVICH, A. L., WEAVER, R. P. & ZHANG, Q. 1999 Richtmyer–Meshkov instability growth: experiment, simulation and theory. *J. Fluid Mech.* **389**, 55–79.

HUERTE RUIZ DE LIRA, C., VELIKOVICH, A. L. & WOUCHUK, J. G. 2011 Analytical linear theory for the interaction of a planar shock wave with a two- or three-dimensional random isotropic density field. *Phys. Rev.* E **83**, 056320.

JACOBS, J. W. 1993 The dynamics of shock accelerated light and heavy gas cylinders. *Phys. Fluids* A **5**, 2239–2247.

JACOBS, J. W., JENKINS, D. G., KLEIN, D. L. & BENJAMIN, R. F. 1995 Nonlinear growth of the shock-accelerated instability of a thin fluid layer. *J. Fluid Mech.* **295**, 23–42.

JACOBS, J. W., KLEIN, D. L., JENKINS, D. G. & BENJAMIN, R. F. 1993 Instability growth patterns of a shock-accelerated thin fluid layer. *Phys. Rev. Lett.* **70**, 583–586.

JACOBS, J. W. & KRIVETS, V. V. 2005 Experiments on the late-time development of single-mode Richtmyer–Meshkov instability. *Phys. Fluids* **17**, 034105.

JACOBS, J. W. & SHEELEY, J. M. 1996 Experimental study of the Richtmyer–Meshkov instability of incompressible fluids. *Phys. Fluids* **8**, 405–415.

JONES, M. A. & JACOBS, J. W. 1997 A membraneless experiment for the study of Richtmyer–Meshkov instability of a shock-accelerated gas interface. *Phys. Fluids* **9**, 3078–3085.

KEANE, R. D. & ADRIAN, R. J. 1990 Optimization of particle image velocimeters. Part 1. Double pulsed systems. *Meas. Sci. Technol.* **1**, 1202–1215.

KEANE, R. D. & ADRIAN, R. J. 1991 Optimization of particle image velocimeters. Part 2. Multiple pulsed systems. *Meas. Sci. Technol.* **2**, 963–974.

KIFONIDIS, K., PLEWA, T., SHECK, L., JANKA, H.-T. & MÜLLER, E. 2006 Non-spherical core collapse supernovae. *Astron. Astrophys.* **453**, 661–678.

KOLEV, T. V. & RIEBEN, R. N. 2009 A tensor artificial viscosity using finite element approach. *J. Comput. Phys.* **228**, 8336–8366.

KRECHETNIKOV, R. 2009 Rayleigh–Taylor and Richtmyer–Meshkov instabilities of flat and curved interfaces. *J. Fluid. Mech.* **625**, 387–410.

LAYZER, D. 1955 On the instability of superposed fluids in a gravitational field. *Astrophys. Rev. J.* **122**, 1–12.

LIKHACHEV, O. A. & JACOBS, J. W. 2005 A vortex model for Richtmyer–Meshkov instability accounting for finite Atwood number. *Phys. Fluids* **17**, 031704.

LIU, B. Y. H. & LEE, K. W. 1975 An aerosol generator of high stability. *Am. Ind. Hyg. Assoc.* **36**, 861–865.

LOMBARDINI, M., HILL, D. J., PULLIN, D. I. & MEIRON, D. I. 2011 Atwood ratio dependence of Richtmyer–Meshkov flows under reshock conditions using large-eddy simulations. *J. Fluid Mech.* **670**, 439–480.

MARIANI, C., VANDENBOOMGAERDE, M., JOURDAN, G., SOUFFLAND, D. & HOUAS, L. 2008 Investigation of the Richtmyer–Meshkov instability with stereolithographed interfaces. *Phys. Rev. Lett.* **100**, 254503.

MATSUOKA, C., NISHIHARA, K. & FUKUDA, Y. 2003 Nonlinear evolution of an interface in the Richtmyer–Meshkov instability. *Phys. Rev.* E **67**, 036301.

MCFARLAND, J. A., GREENOUGH, J. A. & RANJAN, D. 2011 Computational parametric study of a Richtmyer–Meshkov instability for an inclined interface. *Phys. Rev.* E **84**, 026303.

MESHKOV, E. E. 1969 Instability of the interface of two gases accelerated by a shock wave. *Izv. Akad. Nauk. SSSR Maekh. Zhidk. Gaza.* **4**, 151–157.

MEYER, K. A. & BLEWETT, P. J. 1972 Numerical investigation of the stability of a shock-accelerated interface between two fluids. *Phys. Fluids* **15**, 753–759.

MIKAELIAN, K. O. 2003 Explicit expressions for the evolution of single-mode Rayleigh–Taylor and Richtmyer–Meshkov instabilities at arbitrary Atwood numbers. *Phys. Rev.* E **67**, 026319.

MIRELS, H. 1956 Attenuation in a shock-tube due to unsteady-boundary-layer action. *NACA* TN3278.

MIRELS, H. & BRAUN, W. H. 1957 Nonuniformities in shock-tube flow due to unsteady-boundary-layer action. *NACA* TN4021.

MOTL, B., NIEDERHAUS, J., RANJAN, D., OAKLEY, J., ANDERSON, M. & BONAZZA, R. 2007 Experimental studies for ICF related Richtmyer–Meshkov instabilities. *Fus. Sci. Tech.* **52**, 1079–1083.

NISHIHARA, K., WOUCHUK, J. G., MATSUOKA, C., ISHIZAKI, R. & ZHAKHOVSKY, V. V. 2010 Richtmyer–Meshkov instability: theory of linear and nonlinear evolution. *Phil. Trans. R. Soc.* A **368**, 1769–1807.

ORON, D., ARAZI, L., KARTOON, D., RKANATI, A., ALON, U. & SHVARTS, D. 2001 Dimensionality dependence of the Rayleigh–Taylor and Richtmyer–Meshkov instability late-time scaling laws. *Phys. Plasmas* **8**, 2108–2115.

PENG, G., ZABUSKY, N. J. & ZHANG, S. 2003 Vortex-accelerated secondary baroclinic vorticity deposition and late-intermediate time dynamics of a two-dimensional Richtmyer–Meshkov interface. *Phys. Fluids* **15**, 3730–3744.

PRASAD, J. K., RASHEED, A., KUMAR, S. & STURTEVANT, B. 2000 The late-time development of the Richtmyer–Meshkov instability. *Phys. Fluids* **12**, 3730–3744.

RAFFEL, M., KOMPENHANS, J. & WILLERT, C. E. 1998 *Particle Image Velocimetry: A Practical Guide*. Springer.

RAYLEIGH, LORD 1900 *Investigation of the Character of the Equilibrium of an Incompressible Heavy Fluid of Variable Density*. Cambridge University Press.

RICHTMYER, R. D. 1960 Taylor instability in shock acceleration of compressible fluids. *Commun. Pure Appl. Math.* **23**, 297–319.

ROSHKO, A. 1960 On flow duration in low-pressure shock tubes. *Phys. Fluids* **3**, 835–842.

SADOT, O., EREZ, L., ALON, U., ORON, D., LEVIN, L. A., EREZ, G., BEN-DOR, B. & SHVARTS, D. 1998 Study of nonlinear evolution of single-mode and two-bubble interaction under Richtmyer–Meshkov instability. *Phys. Rev. Lett.* **80**, 1654–1657.

SCHLICHTING, H. & GERSTEN, K. 2000 *Boundary-Layer Theory*, 8th edn. Springer.

SCHILLING, O., LATINI, M. & DON, W. S. 2007 Physics of reshock and mixing in single-mode Richtmyer–Meshkov instability. *Phys. Rev.* E **76**, 026319.

SHARP, R. W. JR & BARTON, R. T. 1981 Hemp advection model. UCID-17809 Rev.1, Lawrence Livermore Laboratory.

SOHN, S.-I. 2011 Inviscid and viscous vortex models for Richtmyer–Meshkov instability. *Fluid Dyn. Res.* **43**, 065506.

TAYLOR, G. I. 1950 The instability of liquid surfaces when accelerated in a direction perpendicular to their planes. Part 1. *Proc. R. Soc.* A **201**, 192–196.

THORNBER, B., DRIKAKIS, D., YOUNGS, D. L. & WILLIAMS, R. J. R. 2011 Growth of a Richtmyer–Meshkov turbulent layer after reshock. *Phys. Fluids* **23**, 095107.

TOMKINS, C., KUMAR, S., ORLICZ, G. & PRESTRIDGE, K. 2008 An experimental investigation of mixing mechanisms in shock-accelerated flow. *J. Fluid Mech.* **611**, 131–150.

VON KÁRMÁN, T. 1921 Laminar and turbulent friction. *Z. Angew. Math. Mech.* **1**, 233–252.

VANDENBOOMGAERDE, M., GAUTHIER, S. & MÜGLER, C 2002 Nonlinear regime of a multimode Richtmyer–Meshkov instability: a simplified perturbation theory. *Phys. Fluids* **14**, 1111–1122.

VETTER, M. & STURTEVANT, B. 1995 Experiments on the Richtmyer–Meshkov instability of an air/SF_6 interface. *Shock Waves* **4**, 247–252.

WESTERWEEL, J. 1993 Digital particle image velocimetry, theory and application. PhD thesis, Technische Universiteit Delft.

WILKINS, M. L. 1963 Calculation of elastic–plastic flow. UCRL-7322, Lawrence Radiation Laboratory.

WOUCHUK, J. G. & NISHIHARA, K. 1997 Asymptotic growth in the linear Richtmyer–Meshkov instability. *Phys. Plasmas* **4**, 1028–1038.

YANG, J., KUBOTA, Y. & ZUKOSKI, E. E. 1993 Applications of shock-induced mixing to supersonic combustion. *AIAA J.* **31**, 854–862.

ZHANG, Q. & SOHN, S.-I. 1997*a* Nonlinear theory of unstable fluid mixing driven by shock wave. *Phys. Fluids* **9**, 1106–1124.

ZHANG, Q. & SOHN, S.-I. 1997*b* Padé approximation to an interfacial fluid mixing problem. *Appl. Math. Lett.* **10**, 121–127.